Magnetic structure of the swedenborgite CaBa(Co₃Fe)O₇ derived by unpolarized neutron diffraction and spherical neutron polarimetry

N. Qureshi,[1,2,*] M. T. Fernández Díaz,[1] L. C. Chapon,[3] A. Senyshyn,[4] W. Schweika,[5] and M. Valldor[6,2]

[1]*Institut Laue-Langevin, 71 avenue des Martyrs, CS 20156, 38042 Grenoble Cedex 9, France*

[2]*II. Physikalisches Institut, Universität zu Köln, Zülpicher Strasse 77, D-50937 Köln, Germany*

[3]*Diamond Light Source, Chilton, Didcot, Oxfordshire OX11 0QX, United Kingdom*

[4]*Forschungs-Neutronenquelle Heinz Maier-Leibnitz (FRM-II), Technische Universität München,
Lichtenbergstrasse 1, D-85747 Garching b. München, Germany*

[5]*Institut für Festkörperforschung, Forschungszentrum Jülich, D-52425 Jülich, Germany*

[6]*Leibniz Institute for Solid State and Materials Research, Helmholtzstrasse 20, 01069 Dresden, Germany*

We present a study that combines polarized and unpolarized neutrons to derive the magnetic structure of the swedenborgite compound CaBa(Co₃Fe)O₇. Integrated intensities from a standard neutron diffraction experiment and polarization matrices from spherical neutron polarimetry have been simultaneously analyzed revealing a complex order, which differs from the usual spin configurations on a kagome lattice. We find that the magnetic structure is well described by a combination of two one-dimensional representations corresponding to the magnetic superspace symmetry $P2_1'$, and it consists of spins rotating around an axis close to the [110] direction. Due to the propagation vector $\mathbf{q} = (\frac{1}{3}00)$, this modulation has cycloidal and helicoidal character rendering this system a potential multiferroic. The resulting spin configuration can be mapped onto the classical $\sqrt{3} \times \sqrt{3}$ structure of a kagome lattice, and it indicates an important interplay between the kagome and the triangular layers of the crystal structure.

I. INTRODUCTION

Geometric frustration is a fundamental reason for not having a long-range ordered magnetic ground state. Antiferromagnetic lattices of vertex-sharing triangles, e.g., kagome layers or pyrochlore nets, are rarely found in real materials but are perfect examples of magnetic frustration. The magnetic swedenborgites, i.e., structural homologues to the hexagonal mineral SbNaBe₄O₇ (Refs. [1,2]), contain kagome layers and have been subject to recent investigations due to their diverse magnetic properties, e.g., chiral spin liquids in $Y_{0.5}Ca_{0.5}BaCo_4O_7$ (Refs. [3,4]) and YBa(Co₃Fe)O₇ (Ref. [5]) spin-glasses in YBa(Co₄₋ₓZnₓ)O₇ ($x = 0$–3) (Refs. [6,7]) and long-range antiferromagnetic order in CaBa(Co₂Fe₂)O₇ (Ref. [8]). By slight structural distortions away from the hexagonal symmetry, the geometrical frustration is released. However, as a consequence, there are several different, similarly strong, competing spin interactions, and the resulting ground state is sensitive to the nature of each type of structural distortion. For example, the orthorhombic distortion in CaBaCo₄O₇ results in a ferrimagnetic-like ground state [9,10], while a different orthorhombic distortion in YbBaCo₄O₇₊δ allows for an antiferromagnetic state to evolve [11]. In previous reports, CaBa(Co₃Fe)O₇ was stated to have a hexagonal crystal structure, as based on x-ray diffraction data [12]. Later, a long-range magnetic order was observed, but the spin structure

could not be solved from the obtained data [13], and the reason for the release of geometric frustration was not obvious. As the spins are Heisenberg-like, a Néel order is not expected unless a significant magnetic coupling between the kagome layers is at hand. Thus, the position between the planes, denoted $M1$ in Fig. 1, plays an important role for the appearance of long-range magnetic order. Fe carries a large moment and could easily, at the $M1$ site, mediate the spin-to-spin interactions between the layers, resulting in a three-dimensional (3D) spin system. Here, neutron diffraction analyses were performed on CaBa(Co₃Fe)O₇, revealing the structural distortion from hexagonal symmetry and enabling a determination of its spin-ordered antiferromagnetic ground state.

II. EXPERIMENT

Powder samples were obtained through a solid-state reaction between stoichiometric amounts of analytic grade CaCO₃, BaCO₃, Co₃O₄, and Fe₂O₃ in a corundum crucible. The mixture was heated in air twice at 1100 °C with intermediate grinding to ensure sample homogeneity. To obtain an oxygen stoichiometric sample, the second heat step ended with a quenching of the sample from 900 °C by removing the sample from the furnace. As possible oxygen uptakes are reported at temperatures 200–850 °C in air for YBaCo₄O₇₊δ (Ref. [14]), this quenching prevents oxygen absorption and the sample is thus estimated to have 7.00(5) oxygen per formula unit. A relatively large single crystal was mechanically removed from a sample that was rapidly heated to 1200 °C with a subsequent cooling at an approximate rate of 5 °C/min. Judging

*Author to whom all correspondence should be addressed: qureshi@ill.fr

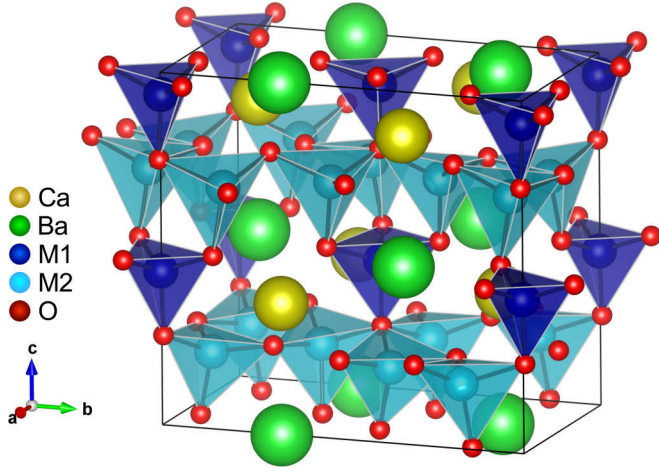FIG. 1. Visualization of the crystal structure of CaBa(Co$_3$Fe)O$_7$ consisting of triangular $M1$ sites (dark blue) and kagome $M2$ sites (light blue), where the latter form the kagome planes within the *a-b* plane.
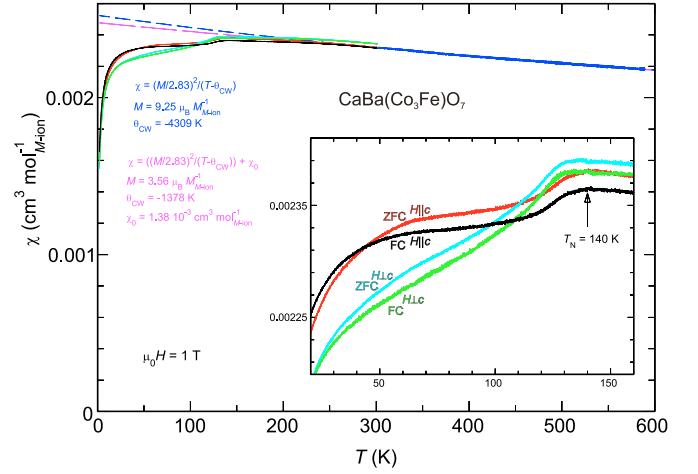

FIG. 2. Magnetic susceptibility measurements in a field of 1 T on single crystalline CaBa(Co$_3$Fe)O$_7$ plotted against temperature. The field-cooled (FC) and zero-field-cooled (ZFC) measurements as well as the direction of the external field in relation to the crystallographic *c* axis are marked and also presented in different colors. The high-temperature data were only obtained for $H \parallel c$ in ZFC mode.

from the crystal's dendritic morphology and pointy end, a self-flux mediation with spontaneous nucleation is assumed to be the growth mechanism. The use of a corundum crucible seems important, as several crystals grew directly on its walls. However, by elemental analysis (EDX in a Philips scanning electron microscope), Al was not detected in crystals or powders. All magnetic measurements were done with a vibrating sample magnetometer (VSM, 40 Hz, 2 mm) in a physical property measurement system (PPMS, Quantum Design). For the temperature-dependent measurement, 1 T was applied. Subsequent magnetizations at chosen temperatures were done in fields up to 14 T. Electric resistivity was measured on a regularly shaped, sintered, polycrystalline piece by the four-contact technique. The gold contacts were attached with silver glue and the sample with holder was slowly cooled by lowering it into a dewar with liquid helium. The sample temperature, as measured by a thermocouple next to the sample, was continuously recorded as a function of resistivity using an in-house setup. Powder neutron diffraction data were obtained at SPODI [15] (FRM II, Munich, Germany) using a constant wavelength of 2.537 Å. About 20 g of sample powder was placed in a sample holder of vanadium, and the cryostat walls were all of aluminum. Helium was used as a cooling agent in a top-loading closed-cycle refrigerator from Vericold. Neutron powder diffraction with polarization analysis was performed at the DNS instrument [16] (FRM II, Munich, Germany). Polarized neutrons with a wavelength of 4.75 Å were applied with polarization analysis to separate the magnetic scattering from the nuclear contribution. Temperatures from 1.2 K up to 300 K were used and controlled by a steady flow of He. The neutron single-crystal diffraction experiment was carried out at the D15 diffractometer (ILL, Grenoble) in the four-circle geometry. A wavelength of 1.17 Å was used from the (331) reflection of the Cu monochromator. All integrated intensities were corrected for absorption applying the transmission factor integral exp$[-\mu(\tau_{\text{in}} + \tau_{\text{out}})]$ by using subroutines of the CAMBRIDGE CRYSTALLOGRAPHIC SUBROUTINE LIBRARY [17] [τ_{in} and τ_{out} represent the path lengths of the beam inside

the crystal before and after the diffraction process, and μ is the linear absorption coefficient, which is 0.064 mm^{-1} for CaBa(Co$_3$Fe)O$_7$]. Spherical neutron polarimetry (SNP) was performed on the spin-polarized hot-neutron diffractometer D3 (ILL, Grenoble), where a monochromatic and polarized neutron beam of wavelength $\lambda = 0.825$ Å was selected by the (111) reflection of a Cu$_2$MnAl Heusler monochromator. The CRYOgenic Polarization Analysis Device [18] (CRYOPAD) was used together with the Cryocradle setup in order not to be limited to a single scattering plane. The sample was mounted with the *b* axis along the vertical axis of the diffractometer with all Cryocradle angles at zero. The nine entries of the polarization matrices were recorded by measuring the polarization [$P = \frac{n^\uparrow - n^\downarrow}{n^\uparrow + n^\downarrow}$, with $n^\uparrow$ ($n^\downarrow$) the number of spin-up (spin-down) neutrons] for an initial neutron polarization along the x, y, or z axis and by analyzing the final neutron polarization components after the scattering process along these directions (the standard local coordination system has been employed, where **x** is parallel to the scattering vector **Q**, **z** is the vertical direction of the diffractometer, and **y** completes the right-handed coordination system). The final neutron polarization was analyzed using a ^{3}He spin filter, whose efficiency was tested regularly by measuring the P_{zz} element of a nuclear Bragg reflection. The observed data were corrected for the time-dependent spin filter efficiency, and the initial neutron polarization of $p_0 = 0.935$ was taken into account for all calculations.

III. RESULTS AND DISCUSSION

A. Macroscopic properties

The temperature dependence of the magnetic susceptibility, $\chi(T)$, of the title phase between 400 and 600 K might be mistaken for paramagnetic behavior, but a simple Curie-Weiss fit (dashed lines in Fig. 2) reveals a very negative Weiss temperature ($\theta_{\text{CW}} = -4.3 \times 10^3$ K), and a far too high moment
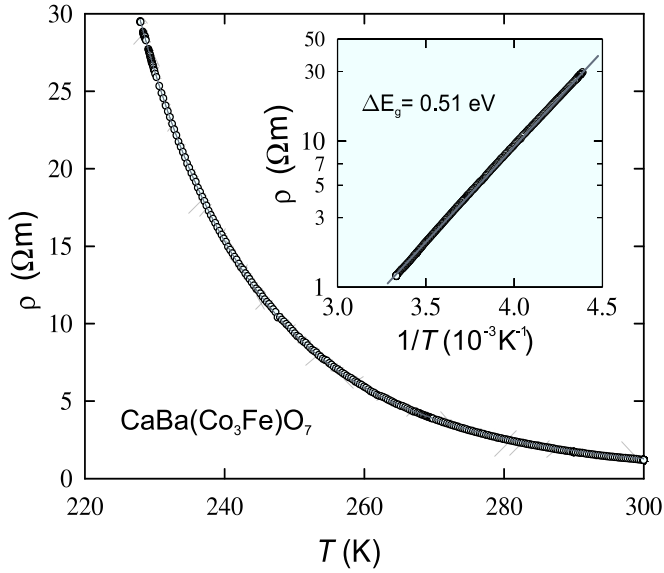
FIG. 3. Electronic resistivity of a sintered CaBa(Co$_3$Fe)O$_7$ polycrystalline sample as a function of temperature. The inset displays an Arrhenius plot with a fit function to extract the activation gap.

per magnetic ion (9.3μ_B) was obtained, where 4.4μ_B is expected for the mean of involved high-spin ions. Even an approximation with a refined constant (χ_0) does not give a physically meaningful paramagnetic behavior: χ_0 is positive and relatively large and infers a strong van Vleck contribution of excited spin states and/or Pauli paramagnetism from conducting electrons, of which both are highly unlikely. However, θ_{CW} and the magnetic moment per ion are relatively smaller and reasonable. Yet, the Weiss constant ($\theta_{CW} = -1.4 \times 10^3$ K) suggests that extremely strong antiferromagnetic spin-spin interactions occur and that it is necessary to measure at higher temperatures to reach truly paramagnetic behavior. Close to $T_N = 140$ K there is a kink in all curves that implies an antiferromagnetic ordering. Below T_N, a minor anisotropy in $\chi(T)$ is seen that could be explained if the mean spin ordering orientation is perpendicular to the c axis, because $H \perp c$ curves are found below $H \parallel c$ curves. For a zero-field-cooled (ZFC) sample, a slight kink can be observed in the $H \parallel c$ data around 65 K, which might originate from a subtle spin reorientation transition. The title compound exhibits typical semiconducting behavior (Fig. 3). The estimated electron conduction activation is about 0.5 eV, which corresponds to the lowest possible band gap: the optical band gap could be significantly larger, and the observed value is then a result of electron hopping between impurity states. The low electron conduction removes Pauli paramagnetism as an explanation for the unusually large χ_0 in the fitted, modified Curie-Weiss approximation, but it suggests strong electron correlations and supports the observation of localized magnetic moments.

B. Nuclear structure

Due to the absence of magnetic scattering on integer positions in reciprocal space (derived from powder neutron experiments, see Fig. 4, and from SNP on reflections with
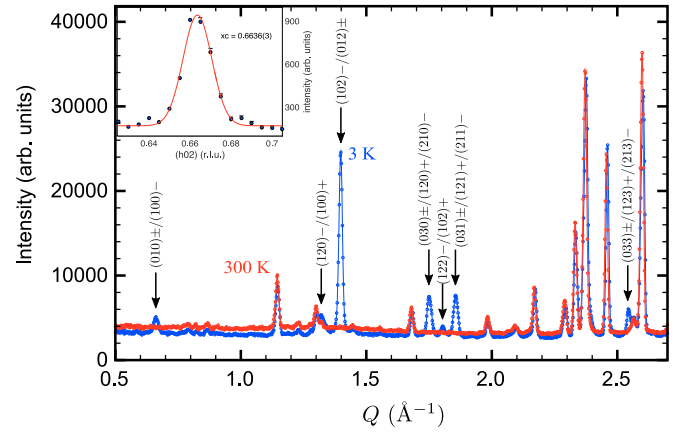

FIG. 4. Powder neutron diffraction data at 300 K (red) and 3 K (blue). The arrows mark the magnetic peaks that could be indexed with a propagation vector $\mathbf{q} = (1/300)$. No additional magnetic scattering can be found on the integer Bragg peaks. The inset shows a reciprocal space scan along the a^* direction recorded using a single crystal.

integer indices, see Sec. III C), the nuclear structure has been investigated within the magnetic phase, at 10 K, by collecting a set of 1472 integer (hkl) reflections (473 unique) from a single-crystal sample corresponding to the $Pbn2_1$ space group. The structural data have been analyzed using the FULLPROF [19] program by refining the positions and the isotropic temperature factor of all species as well as the Co/Fe ratio of the involved sites. Extinction effects were corrected by an empirical ShelX-like model implemented in FULLPROF. Due to the large number of free parameters—resulting from 13 atomic sites without symmetry restrictions concerning the atomic positions—the isotropic temperature factors have been constrained to the same value for Ca/Ba, for Co/Fe on all sites, for O2/O3/O4 (oxygen solely connecting M2 ions), and for O5/O6/O7 (oxygen ions connecting M1 with M2 positions situated above M1). The results are in agreement with the swedenborgite structure and are shown in Table I. The lattice constants obtained from the powder measurement are $a = 6.3145(1)$ Å, $b = 11.0054(1)$ Å, and $c = 10.2194(1)$ Å, which corresponds to a distortion from the hexagonal lattice by less than 0.2°. The temperature factor of O1 is smaller with respect to the other oxygen sites, as one would expect as O1 is shared by three MO$_4$ tetrahedra. The Fe ions preferably occupy the triangular $M1$ site, while the overall Co:Fe ratio averaged over the four sites is 2.92(4):1.08(4), which is in fair agreement with the nominal stoichiometry of 3:1. Note that the Co:Fe ratio was constrained to the same value for the sites within the kagome layer. We have considered the possibility of a twinned sample due to the fact that the high-temperature phase might be hexagonal, which would result in three 120° twins. Indeed, the χ^2 value could be reduced from 6.1 to 3.2 by refining the populations of those three twins resulting in a nearly equal distribution (see Table I). It has to be noted that a similar agreement can be achieved by supposing only two twins, since from the three possible reflections contributing to one observation, two are equivalent in the orthorhombic setting for a big part of the strong reflections [e.g., (260), (2$\bar{6}$0), and ($\bar{4}$00)]. In that case,

TABLE I. Refined nuclear structure parameters within the $Pbn2_1$ space group at 10 K ($R_F = 9.6$, $\chi^2 = 3.2$). The only Wyckoff site in this space group is the general $4a$ site. The twin populations refer to the identity twin and the ones related by the rotation axes 3_1 and 3_2, respectively. The extinction parameters x_{ii} are the diagonal entries of a tensor used to calculate the extinction factor.

Atom	x	y	z	B (Å^2)	occ.
Ca	−0.011(3)	0.667(1)	0.873(3)	0.1(1)	1
Ba	−0.014(3)	0.667(1)	0.500(3)	0.1(1)	1
Co1/Fe1	−0.003(4)	0.001(1)	0.937(2)	0.03(8)	0.49(2):0.51(2)
Co2/Fe2	−0.015(2)	0.169(1)	0.686(3)	0.03(8)	0.81(1):0.19(1)
Co3/Fe3	0.243(2)	0.085(2)	0.1884(4)	0.03(8)	0.81(1):0.19(1)
Co4/Fe4	0.264(2)	0.919(2)	0.678(2)	0.03(8)	0.81(1):0.19(1)
O1	−0.007(1)	0.003(1)	0.254(2)	0.4(1)	1
O2	−0.0013(7)	0.491(1)	0.223(2)	0.96(8)	1
O3	0.767(2)	0.253(25)	0.763(3)	0.96(8)	1
O4	0.735(2)	0.758(1)	0.214(3)	0.96(8)	1
O5	0.050(1)	0.153(1)	0.499(3)	0.82(8)	1
O6	0.207(1)	0.105(1)	−0.003(3)	0.82(8)	1
O7	0.261(1)	0.950(1)	0.499(3)	0.82(8)	1

Twin populations: 0.373(3), 0.302(3), 0.325(3)
Extinction parameters: $x_{11} = 0.002(2)$, $x_{22} = 0.000(1)$, $x_{33} = 0.0033(7)$

the population of the two twins was found to be in the ratio 1:2, as one would expect.

C. Magnetic structure

Short-range magnetic order is obvious already far above the observed Néel temperature ($T_N = 140$ K): Already at 200 K, significant diffuse magnetic neutron scattering is observed close to $Q = 1.35$ Å^{-1} (Fig. 5), which turns into resolution-limited long-range order below 135 K, agreeing with the antiferromagnetic ordering temperature obtained by specific heat [13] and magnetic susceptibility (Fig. 2).
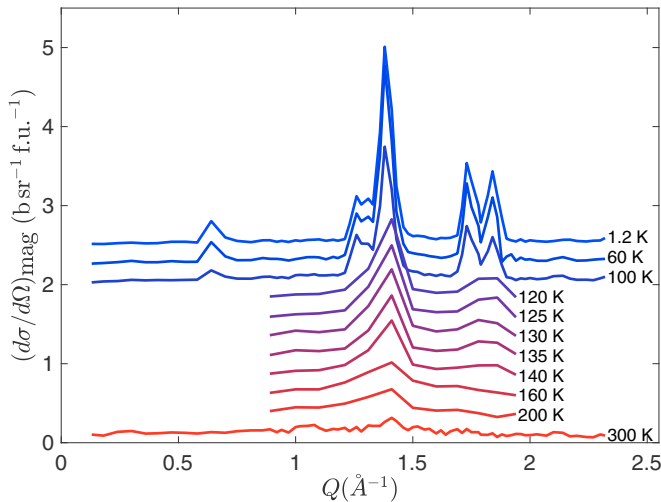

FIG. 5. Magnetic diffuse neutron scattering data on CaBa(Co$_3$Fe)O$_7$ powder as a function of $Q = 2/d$ (d is the interlayer spacing). The curves are plotted in different colors, depending on temperature, as indicated in the graph, and the intensity is directly proportional to the squared scattering factor. Each data set below 300 K is offset by 0.25 b sr^{-1} f.u.$^{-1}$ with respect to the next higher temperature step. The 1.2 K data are taken from Ref. [13].

The magnetic structure has been investigated at 10 K on the D15 diffractometer. A reciprocal space scan across the strong magnetic (102)-**q** Bragg reflection along the **a*** direction confirms the propagation vector $\mathbf{q} = (\frac{1}{3}00)$. A total of 431 integrated intensities from magnetic Bragg reflections were collected in $P1$ symmetry on (hkl)±**q** positions in reciprocal space. Symmetry-adapted spin configurations were derived using the BASIREPS program yielding the basis vectors ψ_n of the irreducible representations Γ_n shown in Table II. The little group only contains two symmetry operators that are compatible with **q** for which each of the four magnetic M sites splits into two orbits, which are—in principle—symmetry-independent. This leads to two one-dimensional irreducible representations, which can be combined in phase quadrature to a two-dimensional one. Unfortunately, magnetic models with only in-plane components agree poorly with the observations ($R_F > 30$). The resulting magnetic structure models consist of cycloidally modulated spins in the kagome layers and amplitude-modulated spins on the triangular site, where the direction of the latter is along the a axis for ψ_1 and along the b

TABLE II. Basis vectors ψ_n of the irreducible representations Γ_1 and Γ_2 and the mixed representation $\Gamma_1 + \Gamma_2$ for the magnetic sites at given fractional coordinates (x,y,z) associated with a propagation vector $\mathbf{q} = (\frac{1}{3},0,0)$ and a phase shift $a = \exp(i\pi/3)$. The components u, v, and w connected to the spin $S_{\Gamma_n}^{p,r}$ have been refined according to their constraints (an overline indicates a negative number). All components may be complex.

Site p	Atom r	(x,y,z)	ψ_1	ψ_2	$\psi_1 + \psi_2$
$4a$	1	$\begin{pmatrix} x \\ y \\ z \end{pmatrix}$	$\begin{pmatrix} u \\ v \\ w \end{pmatrix}$	$\begin{pmatrix} u \\ v \\ w \end{pmatrix}$	$\begin{pmatrix} u_1 + iu_2 \\ v_1 + iv_2 \\ w_1 + iw_2 \end{pmatrix}$
	2	$\begin{pmatrix} x + 1/2 \\ \overline{y} + 1/2 \\ z + 1/2 \end{pmatrix}$	$a\begin{pmatrix} \overline{u} \\ v \\ \overline{w} \end{pmatrix}$	$a\begin{pmatrix} u \\ \overline{v} \\ w \end{pmatrix}$	$a\begin{pmatrix} \overline{u}_1 + iu_2 \\ v_1 + i\overline{v}_2 \\ \overline{w}_1 + iw_2 \end{pmatrix}$

axis for ψ_2. Given the ambiguity in our results, we decided to investigate the same single crystal using polarized neutrons. In addition to the general law in magnetic neutron scattering that only the perpendicular component of the magnetic structure factor (the magnetic interaction vector $\mathbf{M}_\perp$) contributes to magnetic scattering, neutrons with their polarization axis parallel to $\mathbf{M}_\perp$ will undergo a non-spin-flip (NSF) scattering process, while neutrons with polarization perpendicular to $\mathbf{M}_\perp$ will be scattered with a spin-flip (SF). In chiral magnetic structures where the Fourier coefficients of the magnetic moments are imaginary and the real and imaginary parts are perpendicular to each other, chiral scattering can occur. This scattering is polarization-dependent and will create additional polarization along the scattering vector $\mathbf{Q}$ and can therefore be revealed by analyzing the final neutron polarization along the $\mathbf{x}$ direction. As the magnetic Bragg peaks are found as satellites around the nuclear Bragg peaks, we can ignore the nuclear-magnetic interference scattering and its effect on the neutron polarization. However, it has to be taken into account that, if the magnetic subgroup is of order n while the paramagnetic group is of order m, m/n magnetic domains (configurational domains) can be observed. In the present case, the order of the paramagnetic space group $Pbn2_1$ is 4 while the little group is of order 2. However, both symmetry operators that are lost in the transition—the twofold screw axis 2_z and the b glide plane in the y-z plane—transform $+\mathbf{q}$ into $-\mathbf{q}$, which does not result in configurational domains. If the magnetic structure cannot be described by a magnetic space group that is congruent to the one describing the configurational symmetry, then further orientational domains may be present. The orientation of those domains, i.e., their respective $\mathbf{M}_\perp$, with respect to the initial neutron polarization may lead to depolarization of the beam as the initial polarization vector will be rotated differently by the individual magnetic domains. Finally, chirality domains have to be considered for chiral structures. The nine entries of the polarization matrix were measured for eight different magnetic Bragg reflections (note that we have verified the absence of $\mathbf{q} = \mathbf{0}$ magnetic scattering by confirming that the polarization matrices of integer reflections are the identity matrix), from which we will use $(\bar{1}00)$-$\mathbf{q}$ to illustrate the deducible symmetry constraints. As can be seen from Table II, the n glide plane leads to a translation of $a/2$ along the direction of propagation and therefore to a phase shift of $\exp[-i\pi(h \pm q_{a^*})]$ in the magnetic structure factor between atom 1 and atom 2 for all $(h00)\pm\mathbf{q}$ reflections. In addition, the magnetic moment on atom 2 has a phase shift of $a = \exp(i\pi/3)$ for $+\mathbf{q}$, while for $-\mathbf{q}$ the complex conjugate has to be employed. Therefore, in order to produce nonzero components in the magnetic structure factors, the spin components (uvw) of atom 2 must be antiparallel to those of atom 1 (before the application of the phase shift a) yielding magnetic structure factors of the form $(u0w)$ or $(0v0)$ for the irreducible representations Γ_1 or Γ_2, respectively. Figure 6 illustrates that the magnetic interaction vectors $M_\perp$ will be parallel to either the local y or the local z axis for Γ_1 or Γ_2, respectively. In the first case, this would lead to polarization matrix elements $P_{yy} = -P_{zz} = 0.935$, while for the latter one obtains $P_{yy} = -P_{zz} = -0.935$ (taking into account the initial neutron polarization $p_0 = 0.935$ and 100% spin-filter efficiency). However, this does not agree with the observed polarization matrix of the $(\bar{1}00)$-$\mathbf{q}$ reflection yielding $P_{yy} =$

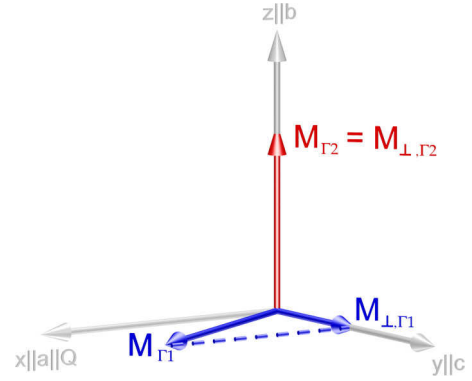FIG. 6. Sketch of the magnetic structure factors ($\mathbf{M}_{\Gamma 1}$, $\mathbf{M}_{\Gamma 2}$) and magnetic interaction vectors ($\mathbf{M}_{\perp,\Gamma 1}$, $\mathbf{M}_{\perp,\Gamma 2}$) for $(h00)\pm\mathbf{q}$ reflections (b axis of the sample vertical) and the two different irreducible representations Γ_1 and Γ_2. Note that for a mixed representation $\Gamma_1 + \Gamma_2$, the magnetic interaction vector $\mathbf{M}_{\perp,\Gamma 1+\Gamma 2}$ lies within the yz plane.

$-0.25(5)$ and $P_{zz} = 0.32(8)$ (after correcting for the spin-filter efficiency). The reduced polarization values in these channels indicate that SF and NSF scatterings partially compensate each other and that the magnetic interaction vector needs to have both a y and a z component, which therefore leads to the conclusion that a further reduction of symmetry is present. Consequently, we have employed a combination of the two irreducible representations ($\Gamma_1 + \Gamma_2$) to analyze the magnetic structure, where the u and w coefficients transform according to Γ_1 and the v coefficients according to Γ_2.

Due to the complexity of the magnetic structure, we have employed a joint refinement of the magnetic structure parameters based on the SNP data and the integrated intensities by minimizing the function

$$\chi^2 = w_\chi \chi_{\text{int}}^2 + (1 - w_\chi)\chi_{\text{SNP}}^2, \qquad (1)$$

where χ_{int}^2 and χ_{SNP}^2 are the respective χ^2 values of the integrated intensities and the polarization matrix entries (MAG2POL, a unique program specially developed for this task, has been used for this purpose [20]). Due to the large amount of information contained in a single polarization matrix (essentially a magnetic structure can be unambiguously determined from two complete polarization matrices obtained from two different sample orientations), the weighting factor w_χ was chosen to be 0.2, which reflects the *information ratio* 4:1 between eight polarization matrices and an integrated intensity data set. Note that SNP is very sensitive to the magnetic moment orientation but not to the amplitude, for which this information is entirely extracted from the integrated intensities. In a first step, the refined parameters were the real and imaginary Fourier components together with their phase shift for the eight different M sites as well as the population of the four possible magnetic domains (two orientational and two chiral domains). An average magnetic form factor was used for each site by taking into account an even mixture between bivalent and trivalent ions as well as the respective Co:Fe ratio. The nuclear structure parameters and the twin populations were fixed, whereas for the latter the no-twin (four magnetic domains in total), the two-twin (eight magnetic domains in total),

TABLE III. Results of the correlated refinement between the SNP data and the integrated intensities ($\chi^2 = 2.0$). Atoms 1 and 2 refer to the triangular and the kagome sublattices, respectively. The atoms are listed pairwise related by the twofold screw axis 2_z, which was lost in the magnetic phase transition. The actual spin orientation is obtained by multiplying the phase factor $\exp(i\varphi)$ by the Fourier coefficients $\psi_1 + \psi_2$. In the two-twins scenario, the populations of the orientational domains related by the n glide plane ($x + 1/2$, $\bar{y} + 1/2$, $z + 1/2$) were refined to 0.27(1) and 0.26(1), while those of the respective chiral domains are 0.20(1) and 0.27(1). The obtained values in the three-twins (no-twins) scenario are 0.34(7) [0.258(5)], 0.15(7) [0.242(5)], 0.01(5) [0.231(4)], and 0.50(7) [0.269(4)], respectively.

Atom	Position	ψ_1 (μ_B)	ψ_2 (μ_B)	phase φ
1a	(0.997, 0.001, 0.937)	$\begin{pmatrix} 2.6(1) \\ 0 \\ 2.04(6)i \end{pmatrix}$	$\begin{pmatrix} 0 \\ -2.71 \\ 0 \end{pmatrix}$	0
1b	(0.003, 0.999, 0.437)	$\begin{pmatrix} 2.59 \\ 0 \\ 2.04i \end{pmatrix}$	$\begin{pmatrix} 0 \\ -2.71 \\ 0 \end{pmatrix}$	$-2\pi/3$
2a	(0.985, 0.169, 0.686)	$\begin{pmatrix} -2.0(1) \\ 0 \\ -1.7(1)i \end{pmatrix}$	$\begin{pmatrix} 0 \\ 2.08 \\ 0 \end{pmatrix}$	0
2b	(0.015, 0.831, 0.186)	$\begin{pmatrix} -1.98 \\ 0 \\ -1.68i \end{pmatrix}$	$\begin{pmatrix} 0 \\ 2.08 \\ 0 \end{pmatrix}$	$-2\pi/3$
2c	(0.243, 0.085, 0.188)	$\begin{pmatrix} -1.98 \\ 0 \\ -1.68i \end{pmatrix}$	$\begin{pmatrix} 0 \\ 2.08 \\ 0 \end{pmatrix}$	$-2\pi/3$
2d	(0.757, 0.915, 0.688)	$\begin{pmatrix} -1.98 \\ 0 \\ -1.68i \end{pmatrix}$	$\begin{pmatrix} 0 \\ 2.08 \\ 0 \end{pmatrix}$	0
2e	(0.264, 0.918, 0.678)	$\begin{pmatrix} -1.98 \\ 0 \\ -1.68i \end{pmatrix}$	$\begin{pmatrix} 0 \\ 2.08 \\ 0 \end{pmatrix}$	$-2\pi/3$
2f	(0.736, 0.082, 0.178)	$\begin{pmatrix} -1.98 \\ 0 \\ -1.68i \end{pmatrix}$	$\begin{pmatrix} 0 \\ 2.08 \\ 0 \end{pmatrix}$	0

and the three-twin scenarios (12 magnetic domains in total) were tested. From the preliminary refinement results, further symmetry constraints considering the Fourier components of the different sites as well as their phases could be deduced: Although the M sites split into two orbits that are related by the twofold screw axis 2_z, the Fourier components of those sites can be constrained to the same values while the phase shift between the magnetic moments can be fixed to $-2\pi/3$. Note that this perfectly matches the magnetic superspace symmetry $P2_1'$, which can be obtained from the program ISODISTORT [21] by mixing the irreducible representations mDT1 ($Pbn'2_1'$) and mDT2 ($Pb'n2_1'$). The magnetic superspace group formalism allows symmetry constraints between magnetic moments that are related by a symmetry operator that transforms $\mathbf{q}$ into $-\mathbf{q}$ by taking into account the connected phase shift, instead of disregarding that symmetry operator and splitting the sites into two orbits, as is the case for standard representation analysis. It was therefore possible to describe both data sets by varying only seven parameters of the magnetic structure: a real ($uu0$)
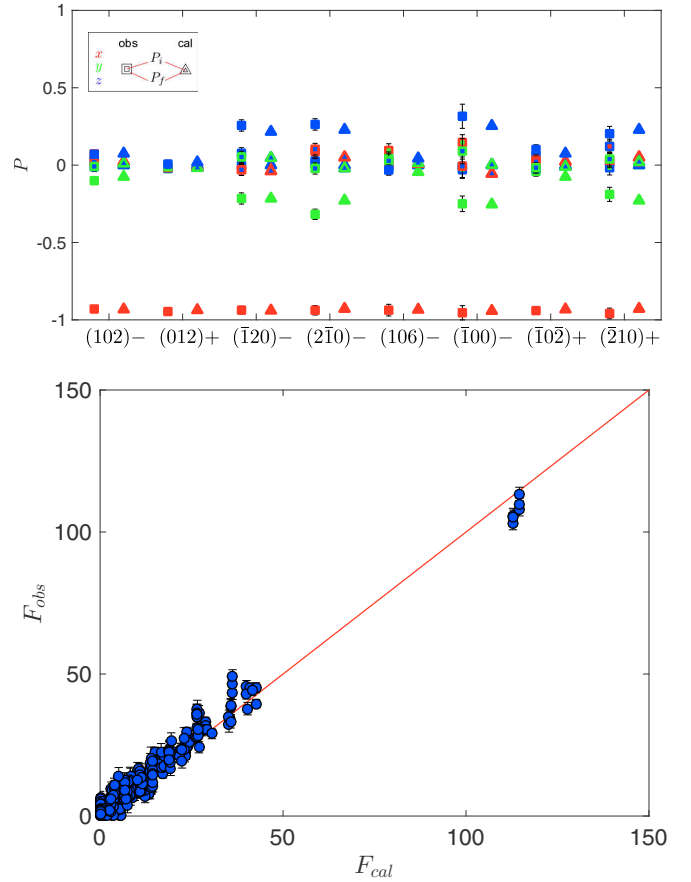

FIG. 7. Upper panel: observed (squares) and calculated (triangles) polarization values of polarization matrices of eight magnetic Bragg peaks. Lower panel: calculated intensities plotted against observed intensities ($R_F = 20.7$). The calculated values of both panels result from a simultaneous fit to the SNP data and integrated intensities ($\chi^2 = 2.0$).

and an imaginary ($00w$) component for the triangular $M1$ sites as well as for the $M2$ sites with three additional parameters for the population of the orientational and chiral domains [$\chi^2 = 2.0$ (combined), $R_F = 20.7$ (integrated intensities only)]. Note that the magnetic moment direction is not along the [$1\bar{1}0$] direction for Fourier coefficients of the type ($u\bar{u}0$) due to the significant difference between the a and b lattice parameters. The agreement with the experimental data is considerably worse for magnetic moments along [$1\bar{1}0$]. The best result has been obtained when constraining the spin component along the b axis to be 5% larger than that along the a axis. Furthermore, we obtain a practically even distribution of the four magnetic domains in the no-twin and two-twin scenarios, which could be expected due to the chiral terms P_{yx} and P_{zx} being close to zero. However, as a matter of fact, the presence of three twins removes the sensitivity of the data to the magnetic domain population, meaning that equally good fits ($\Delta\chi^2 = 0.03$) could be obtained with an even distribution or with the best fit. The results and symmetry constraints are summarized in Table III and Fig. 7 for the two-domain scenario, while the magnetic structure is shown in Fig. 8. Note that the spin configuration is essentially the same within the error bars for all twin scenarios tested.
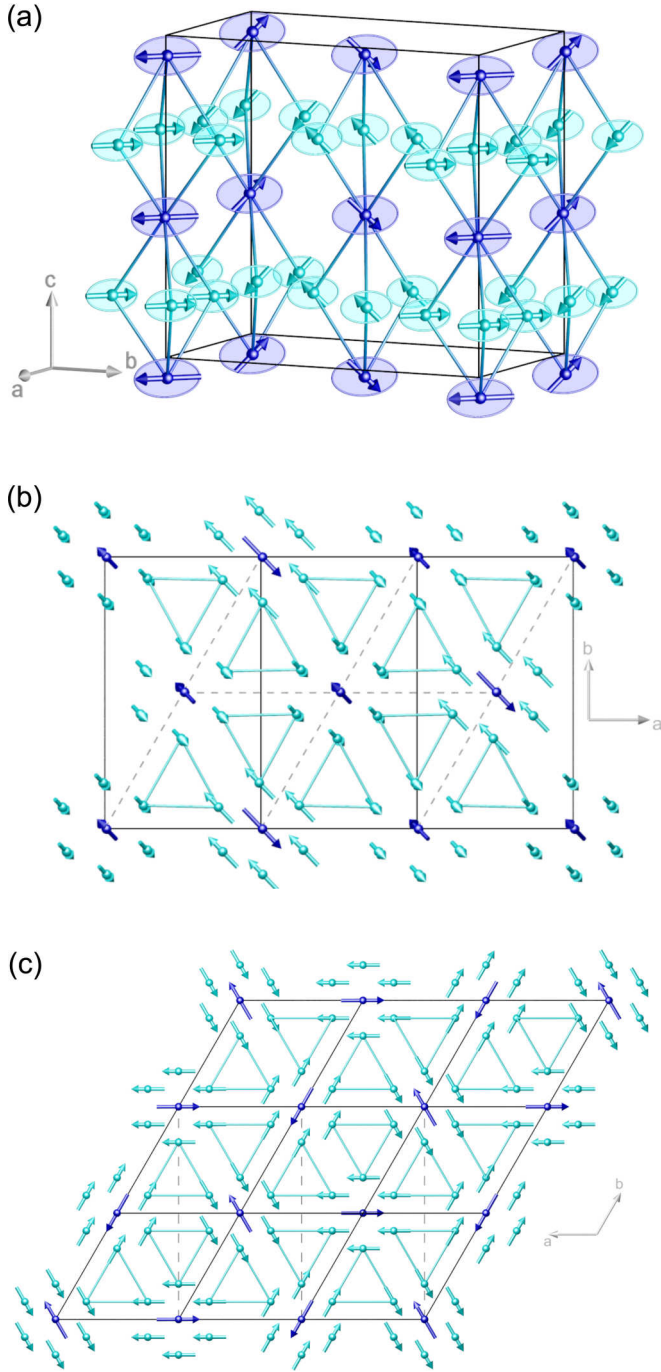
FIG. 8. (a) Perspective view of the magnetic structure in $CaBa(Co_3Fe)O_7$. Only the magnetic ions on the triangular $M1$ (dark blue) and kagome $M2$ sites (light blue) are shown. The spin rotation plane is emphasized by ellipses in the respective colors. Bonds between the two sites are drawn as a guide to the eye. (b) View of one layer of bipyramids along the c axis emphasizing the spin alignment into clusters with a collinear antiferromagnetic configuration within one bipyramid. The (black) solid lines denote the orthorhombic unit cells, while the (gray) broken lines show the related hexagonal lattice. (c) View along the c axis of the classical $\sqrt{3} \times \sqrt{3}$ structure on a hexagonal kagome layer onto which the magnetic structure in (b) can be mapped. The (black) solid lines denote the hexagonal unit cells, while the (gray) broken lines show the related orthorhombic lattice.
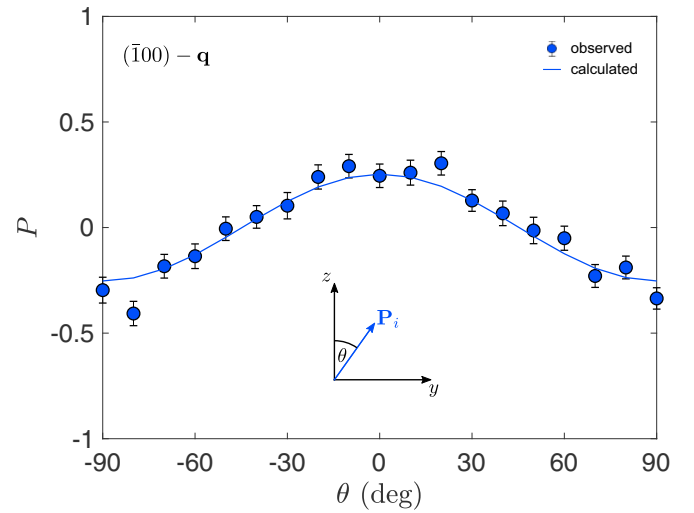

FIG. 9. Polarization values for a rotation of the initial neutron spin component within the local y-z plane and analysis of its longitudinal component after the scattering from the magnetic Bragg reflection $(\bar{1}00)$-$\mathbf{q}$ (θ denotes the angle between the neutron polarization vector and the z axis). The solid line shows the calculation based on the derived magnetic structure.

To further confirm our results, we have carried out a measurement by rotating the initial neutron polarization vector within the local y-z plane and analyzing the longitudinal component after the scattering process at every step. The resulting 180°-periodic curves contain valuable information concerning the spin alignment in the position and in the amplitude of the maxima and minima. Such a rotation from the positive y axis over the z toward the negative y axis has been performed on the $(\bar{1}00)$-$\mathbf{q}$ reflection (see Fig. 9). The observed data were compared to a calculation based on the refined parameters from the joint refinement. One can see that our derived magnetic structure is in excellent agreement with the experimental data. All four magnetic domains (in either
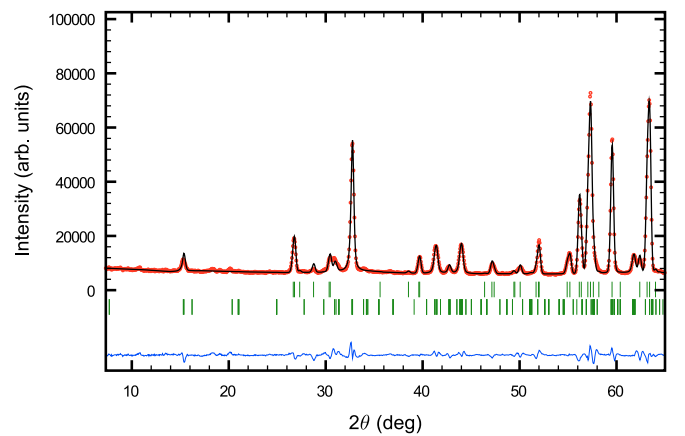

FIG. 10. Observed [(red) dots] and calculated [(black) solid line] diffraction patterns at 3 K with the difference curve shown (in blue) at the bottom. The first row of (green) markers denotes the position of nuclear Bragg peaks within the $Pbn2_1$ space group, while the second row indicates the positions of magnetic Bragg peaks with the propagation vector $\mathbf{q} = (1/3\,0\,0)$.

structural twin scenario) reveal the same P-θ curve for which the respective domain populations were fixed to the values shown in Table III.

The obtained magnetic structure model was then refined to the powder data by using the previously determined symmetry constraints and varying the coefficients of the basis vectors. Figure 10 shows the observed nuclear and magnetic scattering at 3 K and the calculated pattern. The agreement is fairly good ($R_F = 5.5$, magnetic $R_F = 9.2$) and the resulting magnetic structure is qualitatively the same as that obtained from the single-crystal experiments, where the most significant differences concern the c components of both sites. The resulting magnetic moments are [2.25(5) −2.36 2.5(1)i] μ_B and [−2.18(3) 2.29 −1.25(9)i] for the $M1$ and $M2$ sites, respectively.

IV. CONCLUSION

We have presented an extensive study combining heat capacity, susceptibility, powder neutron diffraction, and single-crystal neutron diffraction experiments. For the latter, we have employed a simultaneous analysis of integrated intensities and spherical polarimetry data by refining a global magnetic structure model in a least-squares refinement to both data sets. This allowed us to reveal the complex magnetic structure of the CaBa(Co$_3$Fe)O$_7$ compound, which is different from other members in the swedenborgite family as well as from theoretical predictions. Nevertheless, it is closely related to the classical $\sqrt{3} \times \sqrt{3}$ structure on a kagome lattice and in fact can be mapped to that. For hexagonal swedenborgite compounds, a combination of analytical considerations and classical Monte Carlo methods suggests a collinear in-plane spin alignment within a bipyramidal cluster, which, together with the hexagonal symmetry, leads to a 120° in-plane alignment for $M2$ spins in triangles shared by three bipyramids [22,23]. On the other hand, for CaBaCo$_4$O$_7$, which reveals a gigantic magnetic-field-induced polarization and magnetoelectric coupling [9], the triangular spin configuration has been observed within the bipyramids, moreover with a finite c component [10]. In the orthorhombic compound YBaCo$_4$O$_7$, a $\mathbf{q} = \mathbf{0}$ magnetic structure was reported revealing antiferromagnetically coupled $M1$ spins in the a-b plane and a complex order within the kagome layer [24]. The latter reveals a significant c component, while the in-plane components are reminiscent of the triangular 120° configuration. For the presented compound, which features a commensurate propagation vector $\mathbf{q} = (\frac{1}{3}00)$, typical triangular spin configurations within the kagome pattern in the a-b plane do not explain the experimental data satisfactorily. A careful analysis of the polarization matrices for special magnetic Bragg reflections clearly indicates that the magnetic structure cannot be described by a single irreducible representation of the paramagnetic $Pbn2_1$ space group. Within the Landau theory, the combination of two representations is only allowed for a successive condensation of two order parameters. Indeed, the obtained magnetic space group $P2_1'$ is not a maximal subgroup of $Pbn2_1$ but is obtained by either of the intermediate space groups $Pb'n2_1'$ or $Pbn'2_1'$. An indication for two magnetic phase transitions might be present in our susceptibility data (Fig. 2), where a small kink is observable in the ZFC curve with $H \parallel c$ at a temperature well below

T_N. However, there is no indication of a phase transition at that temperature in the heat-capacity data. Therefore, the only plausible explanation is the presence of two successive magnetic phase transitions in a very narrow temperature range below T_N unresolved by the heat capacity measurements [13]. The mixing of irreducible representations Γ_1 and Γ_2 breaks the n glide plane, and interestingly, it leads to a collinear alignment of spins within one chain of bipyramids along the c axis. From the resulting spin configuration between neighboring $M1$ and $M2$ sites, one can draw important conclusions about the coupling between the triangular and the kagome layers that are decisive for the three-dimensional ordering in the swedenborgite compounds. One can see in Fig. 8(a) that all spins of one bipyramidal chain along the c axis are collinear, with the spins within the triangular plane being antiparallel to those in the kagome plane. As the bond lengths between $M1$-$M2$ nearest neighbors and $M2$-$M2$ nearest neighbors are comparable, the resulting magnetic structure is a strong indication that the predominant exchange interaction is between $M1$ and $M2$ spins along the c axis and that the frustrated in-plane exchange interactions of the $M2$ spins must be weaker. The interaction between the planes was shown not to relieve the frustration within the $M2$ plane, but to act as an external field lifting the ground-state degeneracy [25]. As a result, the system is able to develop long-range magnetic order at a quite elevated temperature. However, there is no clear indication that the magnetic moments would prefer an in-plane component (u_1 u_2 0) instead of the higher symmetry direction [1$\bar{1}$0], but it is in fact similar to the $M1$ ordering pattern in YBaCo$_4$O$_7$ (Ref. [24]). A complex scheme of competing interactions may be responsible for that, especially given the fact that the moment direction changes slightly as a function of temperature in the related compound [24]. The maximum amplitude of the magnetic moments is within the a-b plane and amounts to 3.7(1)μ_B and 2.9(1)μ_B for the $M1$ and $M2$ sites, respectively. The amplitude on the $M1$ site is close to the expected spin value for an even mixture of M^{2+} and M^{3+} ions (high-spin configuration) taking into account the Co:Fe ratio on that particular site, which yields 4.01μ_B. The maximum amplitude on the $M2$ site is considerably smaller than the expected value of 3.69μ_B and therefore indicates a remaining degree of frustration within the kagome layer. When viewed along the c axis [Fig. 8(b)], the clusterlike spin alignment becomes apparent with an antiferromagnetic order between the $M1$ and $M2$ spins within a bipyramid similar to the predictions of Refs. [22] and [23]. However, the striking difference between the proposed structure of CaBa(Co$_3$Fe)O$_7$ and those presented for the swedenborgite family—based on theoretical or experimental work—is the modulation of the spins perpendicular to the kagome layers. In addition to the antiferromagnetic configuration of spins of the same bipyramidal chain, one can see in Fig. 8(b) that those spins belonging to three different chains (shown in triangles) reveal the typical 120° configuration, which is indeed in accordance with the $\sqrt{3} \times \sqrt{3}$ structure on a hexagonal kagome lattice [Fig. 8(c)]. However, instead of rotating around the c axis as in the hexagonal case, the cluster spin-alignment rotates around an axis close to [110]. For Heisenberg spins without single-ion anisotropy, both configurations are in fact energetically equivalent and can be mapped one onto the other. The elliptical

spin rotation plane is described by the Fourier coefficients $(u_1 \; u_2 \; iw_1)$, where the indices 1 and 2 refer to the irreducible representations according to which the components transform and $u_2 = -1.05u_1$. Together with the propagation vector $q = (\frac{1}{3}00)$, this results in a spin modulation that has a cycloidal and a helicoidal character as **q** is neither perpendicular nor within the rotation plane. From the point of view of multiferroics, such a magnetic structure could bear very interesting properties concerning the symmetry-breaking mechanism, which is quite different for cycloidal structures and proper screws. Within one magnetic domain, the handedness of the $M1$ and $M2$ spin chains along the a axis is unique with a continuous rotation for the former and a staggered rotation of the latter where blocks of two parallel spins are present along the chain. The magnetic structure can be described in the magnetic superspace symmetry $P2'_1$, which in principle should allow a ferroelectric polarization along the c axis under the condition that the magnetoelastic coupling is strong enough, which is not necessarily the case as the nuclear structure lacks inversion symmetry already at very high temperatures.

[1] G. Aminoff, Z. Kristallogr. **60**, 262 (1924).

[2] G. Aminoff and R. Blix, Kgl. Sv. Vet. H. **11**, 3 (1933).

[3] M. Valldor, Solid State Sci. **8**, 1272 (2006).

[4] W. Schweika, M. Valldor, and P. Lemmens, Phys. Rev. Lett. **98**, 067201 (2007).

[5] M. Valldor, R. P. Hermann, J. Wuttke, M. Zamponi, and W. Schweika, Phys. Rev. B **84**, 224426 (2011).

[6] M. Valldor and M. Andersson, Solid State Sci. **4**, 923 (2002).

[7] M. Valldor, J. Phys.: Condens. Matter **16**, 9209 (2004).

[8] J. D. Reim, E. Rosén, W. Schweika, M. Neven, N. R. Leo, D. Meiser, M. Fiebig, M. Schmidt, C.-Y. Kuo, T.-W. Pi *et al.*, J. Appl. Cryst. **47**, 2038 (2014).

[9] V. Caignaert, A. Maignan, K. Singh, C. Simon, V. Pralong, B. Raveau, J. F. Mitchell, H. Zheng, A. Huq, and L. C. Chapon, Phys. Rev. B **88**, 174403 (2013).

[10] R. S. Fishman, S. Bordács, V. Kocsis, I. Kézsmárki, J. Viirok, U. Nagel, T. Rõõm, A. Puri, U. Zeitler, Y. Tokunaga *et al.*, Phys. Rev. B **95**, 024423 (2017).

[11] A. Huq, J. F. Mitchell, H. Zheng, L. C. Chapon, P. G. Radaelli, K. S. Knight, and P. W. Stephens, J. Solid State Chem. **179**, 1136 (2006).

[12] M. Valldor, Solid State Sci. **6**, 251 (2004).

[13] M. Valldor, Y. Sanders, and W. Schweika, J. Phys.: Conf. Ser. **145**, 012076 (2009).

[14] M. Karppinen, H. Yamauchi, S. Otani, T. Fujita, T. Motohashi, Y.-H. Huang, M. Valkeapää, and H. Fjellvåg, Chem. Mater. **18**, 490 (2006).

[15] H. Maier-Leibnitz Zentrum, J. Large-scale Res. Facil. **1**, A5 (2015).

[16] H. Maier-Leibnitz Zentrum, J. Large-scale Res. Facil. **1**, A27 (2015).

[17] J. C. Matthewman, P. Thompson, and P. J. Brown, J. Appl. Cryst. **15**, 167 (1982).

[18] E. Lelièvre-Berna, E. Bourgeat-Lami, P. Fouilloux, B. Geffray, Y. Gibert, K. Kakurai, N. Kernavanois, B. Longuet, F. Mantegezza, M. Nakamura *et al.*, Physica B **356**, 131 (2005).

[19] J. Rodríguez-Carvajal, Physica B **192**, 55 (1993).

[20] N. Qureshi, arXiv:1801.08431.

[21] H. T. Stokes, D. M. Hatch, and B. J. Campbell, stokes.byu.edu/isotropy.html.

[22] D. D. Khalyavin, P. Manuel, J. F. Mitchell, and L. C. Chapon, Phys. Rev. B **82**, 094401 (2010).

[23] S. Buhrandt and L. Fritz, Phys. Rev. B **90**, 020403(R) (2014).

[24] D. D. Khalyavin, P. Manuel, B. Ouladdiaf, A. Huq, P. W. Stephens, H. Zheng, J. F. Mitchell, and L. C. Chapon, Phys. Rev. B **83**, 094412 (2011).

[25] P. Manuel, L. C. Chapon, P. G. Radaelli, H. Zheng, and J. F. Mitchell, Phys. Rev. Lett. **103**, 037202 (2009).